



HAL
open science

New, 3D binder-jetted carbons with minimal periodic surface structures

Marco Pelanconi, Pauline Blyweert, Giovanni Bianchi, Vincent Nicolas, Davide Viganò, Samuele Bottacin, Vanessa Fierro, Alain Celzard, Alberto Ortona

► **To cite this version:**

Marco Pelanconi, Pauline Blyweert, Giovanni Bianchi, Vincent Nicolas, Davide Viganò, et al.. New, 3D binder-jetted carbons with minimal periodic surface structures. *Carbon*, 2023, 213, pp.118252. 10.1016/j.carbon.2023.118252 . hal-04274473

HAL Id: hal-04274473

<https://hal.univ-lorraine.fr/hal-04274473v1>

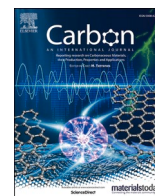
Submitted on 7 Nov 2023

HAL is a multi-disciplinary open access archive for the deposit and dissemination of scientific research documents, whether they are published or not. The documents may come from teaching and research institutions in France or abroad, or from public or private research centers.

L'archive ouverte pluridisciplinaire **HAL**, est destinée au dépôt et à la diffusion de documents scientifiques de niveau recherche, publiés ou non, émanant des établissements d'enseignement et de recherche français ou étrangers, des laboratoires publics ou privés.



Distributed under a Creative Commons Attribution 4.0 International License



New, 3D binder-jetted carbons with minimal periodic surface structures

Marco Pelanconi^a, Pauline Blyweert^b, Giovanni Bianchi^a, Vincent Nicolas^b, Davide Viganò^a,
Samuele Bottacin^a, Vanessa Fierro^b, Alain Celzard^{b,c,**}, Alberto Ortona^{a,*}

^a University of Applied Sciences (SUPSI), Mechanical Engineering and Materials Technology Institute (MEMTI), Polo Universitario Lugano, 6962, Lugano, Switzerland

^b Université de Lorraine, CNRS LJI, F-88000, Epinal, France

^c Institut Universitaire de France (IUF), F-75231, Paris, France

ARTICLE INFO

Keywords:

3D printing
Binder jetting
Carbon monoliths
Graphite
Infiltration

ABSTRACT

This study focuses on the design, additive manufacturing, and characterization of porous carbon-based structures in the form of a triply periodic minimal surface (TPMS) with outstanding mechanical properties and oxidation resistance, combined with good electrical and thermal conductivity. Binder jetting (BJ) of graphite-carbon black powders was used to 3D print computational models of three TPMS with different topologies and geometric porosities. Infiltration and pyrolysis (PIP) with furan resin was then performed to densify the parts. Composite materials, comprising a highly disordered carbon matrix binding well-crystallized graphite grains, were obtained. The printed and pyrolyzed samples are highly porous TPMS cylinders with diameter, height and a surface thickness of ~19 mm, ~33 mm and 0.76 mm, respectively. The samples have a skeleton intrinsic porosity of 20%, of which 8% is open, meaning that the material could potentially be further infiltrated and densified. Nevertheless, the samples have better mechanical properties than compressed carbon-graphite composites, as well as 3D-printed carbon produced by direct ink writing and stereolithography. High-temperature tests showed that, although the amorphous carbon matrix is more prone to oxidation than the graphite grains, the overall oxidation resistance remains exceptionally high. These properties allow for applications as Joule resistors and in seasonal thermal storage.

1. Introduction

Offering great freedom of geometry, precision and repeatability, 3D printing of carbonaceous materials, and even more so of graphite, has attracted considerable interest in recent years [1]. The knowledge and development of processes have enabled the printing of all-carbon materials that meet the requirements of numerous applications in the fields of energy, health and sustainable development [1,2]. Among the various additive manufacturing techniques, binder jetting (BJ) is a technology of choice for 3D printing of graphite architectures. With low unit cost and high build volumes and rates, this technique, which involves the selective deposition of a liquid binder onto a layer of powdered material, is capable of processing a wide range of powders, including those that are difficult to machine or form using traditional manufacturing methods, such as graphite [3]. In addition, BJ-printed parts exhibit good accuracy and fine detail, making it an ideal technique for pharmaceutical and biomedical manufacturing [4,5], energy applications such thick

electrodes [6] or heat exchangers with, for instance, a triply periodic minimal surface (TPMS) structure [7,8]. As the use of graphite in BJ is relatively new, research has focused on optimizing the process when applied to carbon and graphite, as well as improving the mechanical properties of the printed architectures, by varying binder powders, deposition methods, heat treatments and post-processing such as polymer infiltration and pyrolysis (PIP) [9–11].

PIP is a densification process in which a porous preform made of graphitic powder is infiltrated with a pre-carbon polymer, followed by pyrolysis to decompose the polymer and convert it into a dense carbon matrix [12]. In this work, we combine the industrially scalable BJ additive manufacturing process with PIP, which offers unique advantages in terms of the final properties of the components produced.

A recent application of carbon/graphite materials is the thermochemical heat storage for heating buildings in winter, which can be provided by solar thermal energy collected in summer. An interesting approach is sorption storage [13,14]. For example, in the case of

* Corresponding author. SUPSI, MEMTI.

** Corresponding author. Université de Lorraine.

E-mail addresses: alain.celzard@univ-lorraine.fr (A. Celzard), alberto.ortona@supsi.ch (A. Ortona).

<https://doi.org/10.1016/j.carbon.2023.118252>

Received 24 April 2023; Received in revised form 21 June 2023; Accepted 24 June 2023

Available online 1 July 2023

0008-6223/© 2023 The Authors. Published by Elsevier Ltd. This is an open access article under the CC BY license (<http://creativecommons.org/licenses/by/4.0/>).

hydrated salt/water vapor working pair, the efficiency of the system is increased by maximizing the heat transfer in the sorption-desorption unit by a higher difference in concentration of sodium hydroxide (30–50%) and water (NaOH–H₂O) solution between its inlet and outlet during thermal loading and unloading. For this purpose, a large wetted area of the heat exchanger is desirable [15]. Porous bodies have large surface area and are already on the market, but they are not optimized for the NaOH corrosive environment (even at low temperature) of the sorption-desorption unit. Carbon/graphite is an ideal material for this purpose. It is stable in alkaline environments, has good thermal

conductivity, and it can be additively shaped into complex architectures to increase the performance of the heat exchanger.

In this work, we show the possibility to produce complex graphite parts by the additive binder jetting technique. After describing the preparation and characterization procedures, we report the main features of these new materials in terms of composition, porous texture, structure, and surface, mechanical and thermal properties.

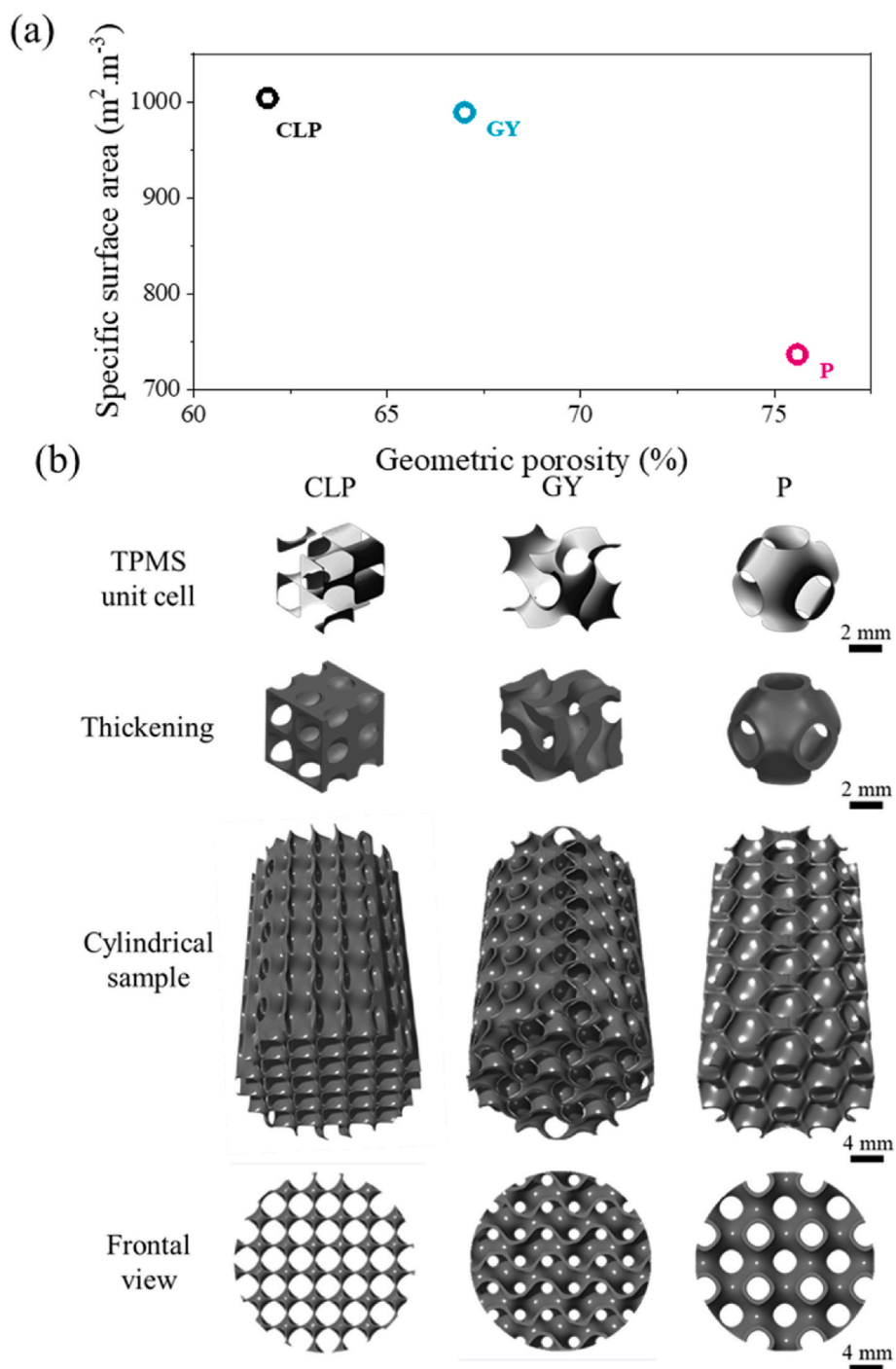


Fig. 1. (a) Geometrical aspect of the TPMS structures; (b) Cylindrical structures based on TPMS sheets designed with a cell size of 6.48 mm and a wall thickness of 0.75 mm: crossed layers of parallels (CLP), gyroid (GY) and primitive (P) from the unit cells (top) to the final solid structures (bottom). (A colour version of this figure can be viewed online.)

2. Materials and methods

2.1. Design of cellular structures

The samples were designed using a specific algorithm developed at SUPSI. The computer design tool was developed in Grasshopper using Rhinoceros software for visualization (McNeel, Seattle, Washington, USA). Three TPMS topologies were investigated in this work, namely Crossed Layers of Parallels (CLP), Gyroid (GY), and Primitive (P) minimal surfaces. The architectures were constructed from a single surface (the unit cell), which was designed by plotting the approximation of the mathematical functions that define the TPMS topology. These minimal surfaces are described by the following equations:

$$CLP = \sin z \bullet \sin y - 0.4 \bullet (\sin x \bullet \cos z \bullet \cos y) \quad \text{Eq. 1}$$

$$GY = \sin x \bullet \cos y + \sin y \bullet \cos z \bullet \sin z \bullet \cos x \quad \text{Eq. 2}$$

$$P = \cos x + \cos y + \cos z \quad \text{Eq. 3}$$

Single unit cells of the TPMS topologies with a cell size of 6.48 mm were then generated and then patterned in three-dimensional space to the desired cylindrical shape with a diameter of 21.6 mm and a length of 37.8 mm. These values were chosen considering the shrinkage of the parts after the PIP process, around 10% according to the authors' preliminary work, to obtain a diameter of 20 mm and a height of around 34 mm, and also to maintain a geometric porosity above 60% to ensure homogeneous infiltration. The three TPMS topologies were used to create sheet-based structures representing the minimal surface, which were thickened to 0.75 mm. This thickness was chosen according to the limitations of the fabrication technique. Due to the different topologies, the combination of cell size and thickness resulted in different geometric porosities (*i.e.*, 1 – relative density) and specific geometric surface areas, which ensure homogeneous infiltration and the production of ceramic parts with the same microstructure after the infiltration/pyrolysis step. The geometric aspects for the samples used in this study are presented in Fig. 1a, and are summarized in Table S1. Fig. 1b shows the single unit cells of each TPMS structure, the thickening of the unit cell and the patterning into the final cylindrical sheet-based structures.

2.2. Manufacturing of TPMS structures

Binder Jetting onto graphite-based powder beds was used to 3D print the numerical domains of Fig. 1. After curing and de-powdering, the preforms were further infiltrated and pyrolyzed to increase their density.

2.2.1. Materials

A mixture of graphite powder (Graphite, Imerys S.A., Switzerland) and 5 vol% of carbon black (CB) (Super P–Li, Imerys S.A., Switzerland) was used for the preparation of the powder bed for 3D printing by binder jetting. CB was added to the graphite in order to improve the wettability of the powders with the phenolic binder, increase the flowability of the powders and improve the mechanical properties of the green part [16–18]. An amount of 5 vol% CB was found to be optimal for high-precision printing compared with the CAD model, whereas a higher concentration gave lower resolution, due to much better wetting of the grains by the resin, resulting in excess thicknesses compared with the CAD model (see Fig. S1). Table 1 shows the main characteristics of the

Table 1
Characteristics of powders.

Powder	True density (g·cm ⁻³)	Tap density (g·cm ⁻³)	Particle size (µm)	BET area (m ² ·g ⁻¹)
Graphite	2.25	1.15	26.1	2.8
Super P–Li CB	1.90	0.16	0.04	62.0

powders, which were dry-mixed using a three-dimensional shaking mixer (Turbula T2F, WAB group, Switzerland), with a rotation speed of 100 rpm and a mixing time of 24 h. The final, true density of the graphite-CB mixture was 2.23 g cm⁻³.

A phenolic binder (FB101 Binder, ExOne, Pennsylvania, USA), containing a mixture of 2-propanol, phenol and formaldehyde, was used as injection binder into the powder by the print heads. Its density was 0.95 g cm⁻³ and its dynamic viscosity was 15 mPa s at 20 °C. For the next step of polymer infiltration, furan resin (FuroLite 100 series Resins, Trans-Furans Chemicals, Geel, Belgium) mixed with 5 wt% of latent catalyst (HM 1448, WIZ chemicals, Dairago, Italy) was employed. The resin and catalyst were mixed with a planetary centrifugal mixer “Thinky Mixer ARE-250” (Thinky U.S.A., INC – U.S.A) at 700 rpm for 3 min. The density and viscosity of the mixture were 1.2 g cm⁻³ and 300 mPa s at 25 °C, respectively. To produce each of the three types of architecture shown in Fig. 1, strictly the same materials and processing methods were used.

2.2.2. 3D printing of the green parts

The preforms were printed using a Binder Jetting 3D printer (Innovent+, ExOne, Pennsylvania, USA), which selectively deposits a liquid polymeric binder onto a bed of carbon powder via an inkjet head. The binder solidifies thanks to an infrared heat source and forms a solid layer. The process is then repeated, building the final object layer by layer. Samples were printed by spreading a 50 µm-thick powder bed. The parameters used for 3D printing are listed in Table 2.

Fig. 2 shows the schematic and principle of the Binder Jetting technology. Once the object was completed, the job box, containing the printed samples and the unbound powder, was heat treated in a drying oven (Binder VD23, BINDER GmbH, Tuttlingen, Germany) at 200 °C in air for 3 h. This step is essential to remove the solvent present in the binder (55 wt%) and to pre-cure the phenolic resin, which ensures sufficient mechanical resistance to handle the part. Excess powder was then removed by carefully scrubbing the samples with a soft brush and blowing their inner surface with an air gun, at low pressure (~0.5 bar). The powder did not aggregate at any stage of the process, and always remained perfectly fluid.

2.2.3. Precursor infiltration and pyrolysis (PIP)

The printed samples were infiltrated with the furan resin using a dipping apparatus developed at SUPSI. It consists of a hermetically sealed vessel containing the liquid carbon precursor in which the component, placed inside a cage, is immersed. Inside the apparatus, vacuum can be created and pressure applied. The infiltration process involved four phases: (i) the sample was first degassed at room temperature for 60 s, (ii) it was then immersed in the liquid carbon precursor and held for 60 s, (iii) atmospheric pressure was restored and the sample was held in the polymer for another 60 s.

Prior to pyrolysis, the samples were centrifuged at 350 rpm for 3 min to drain excess polymer and they were cured at 145 °C for 2 h to promote polymer cross-linking in a vacuum drying oven (Binder VD23, BINDER GmbH, Tuttlingen, Germany). This centrifugation speed was low enough to prevent the liquid resin from escaping from the pores. After infiltration, the samples were heat treated in a furnace (Keos SPS01, Keos, Concorezzo, Italy) in flowing argon (30 L h⁻¹). The steps of the thermal treatment were: (i) from room temperature to 500 °C, with a heating rate of 80 °C h⁻¹, (ii) from 500 °C to 1000 °C, with a heating rate of 51 °C·h⁻¹, (iii) a dwell time of 1 h at 1000 °C, and (iv) a natural cooling

Table 2
Printing parameters.

Parameter	Unit	Value
Binder saturation	%	390
Layer thickness	µm	50
Recoat speed	mm sec ⁻¹	500

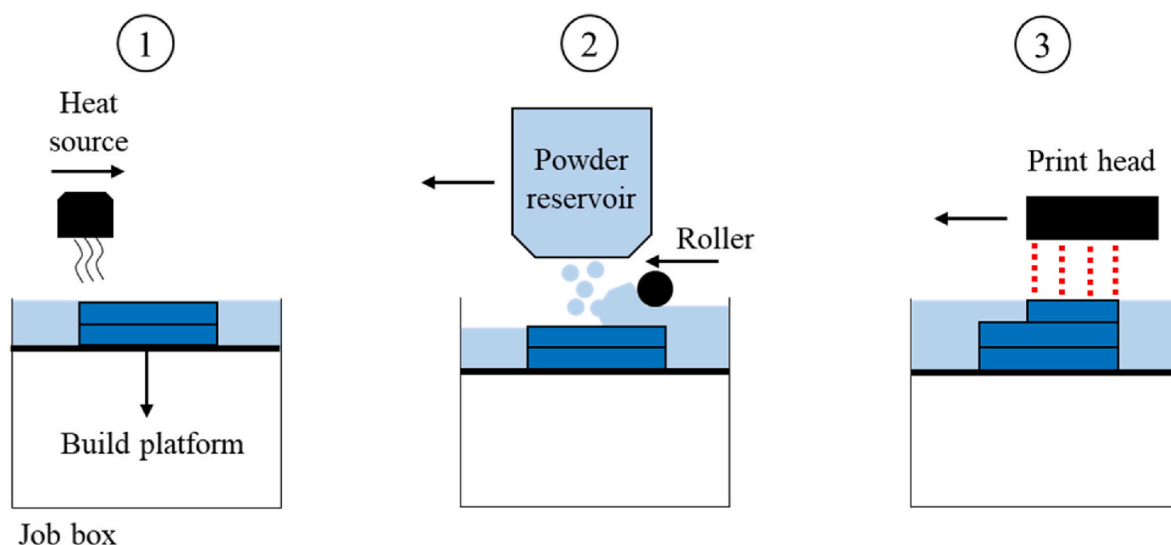


Fig. 2. Schematic and principle of the Binder Jetting technology: (1) heating of the powder layer; (2) deposition of new powder and layering of a specific thickness by the roller; (3) selective jetting of the liquid binder from the print head. (A colour version of this figure can be viewed online.)

to room temperature.

2.3. Characterization

2.3.1. Chemical composition, surface properties and reactivity to hot oxidation

The bulk contents of sulfur, nitrogen, hydrogen and carbon were obtained by elemental analysis (EA) performed in an Elementar Vario EL Cube analyser (Elementar Analysensysteme GmbH, Germany). The oxygen content was calculated by difference.

The yield of amorphous carbon, formed during pyrolysis of the furan resin at 1000 °C under an inert atmosphere, was determined by thermogravimetric analysis (TGA/DSC 3+, Mettler-Toledo GmbH, Greifensee, Switzerland) in argon up to 1000 °C using a flow rate of 50 mL min⁻¹ and a heating rate of 10 °C·min⁻¹. Its bulk density was measured by helium pycnometry (Ultrapyc3000, Anton Paar QuantaTec Inc., Florida, USA).

Water contact angles were measured with a Drop Shape Analyser DSA100 (Krüss, Germany), by depositing 2 µL water drops on top of the sample (either polished or fractured) with an automatic drop deposition system. Contact angles were measured with Krüss software from droplet images captured with a digital camera. The measurements were carried out at 20 °C and 40% relative humidity. Each contact angle was obtained by measuring the angles on the left and right sides of the droplet and taking the average.

Thermal oxidation of carbon samples was studied by thermogravimetric analysis (TGA) under non-isothermal and isothermal conditions using a STA 449 F3 Jupiter® (Netzsch, Germany). For non-isothermal conditions, about 10 mg of the sample was placed in an alumina crucible, and the temperature was increased at a constant heating rate of 15 °C·min⁻¹, from 25 to 1200 °C, under a constant synthetic air flow of 50 mL min⁻¹.

Under isothermal conditions, about 5 mg of sample was heated at a constant heating rate of 10 °C·min⁻¹ from 25 °C to the chosen oxidation temperature under a constant argon flow rate of 50 mL min⁻¹. Argon was then replaced by synthetic air flowing at the same rate of 50 mL min⁻¹, and the temperature was maintained for 2 h. From the non-isothermal curve, oxidation temperatures ranging from 500 to 700 °C were selected, and the samples were oxidized to a weight loss of approximately 15%. According to ASTM 7542-15 [19], the average oxidation rate at a given oxidation temperature was determined by a linear fit of the weight loss plotted against time in the range of 5%–10%

of the oxidation weight loss of the sample and normalised by the sample weight at time t . [20] The activation energy (E_a) and pre-exponential factor (k_0) were estimated from the slope and intercept of the Arrhenius plot, *i.e.*, from the plot of the logarithm of the oxidation rate versus the reciprocal of the absolute temperature.

2.3.2. Morphology and structure

Scanning Electron Microscopy (SEM, GeminiSEM 500, Zeiss GmbH, Germany) was performed to investigate the general morphology of the surface and fractured areas of the 3D-printed carbon using secondary electrons accelerated under 5 kV.

X-ray tomography was performed with an RX Solution tomograph (RX Solution, France) driven by X-Act software. The X-ray source voltage was set to 130 kV and the current to 30 µA, and 2D images with isotropic voxel sizes of 4.9 µm were recorded. The 3D reconstructed images were analysed using ImageJ (open source software).

XRD measurements were performed using a Bruker D8 Advance powder diffractometer (Bruker, U.S) in a Bragg-Brentano reflection configuration. The latter was equipped with a molybdenum anode X-ray source operating at 50 kV and 45 mA. The powdered sample was introduced in a Lindemann capillary, which allows averaging a possible preferential orientation of the grains.

Raman spectra were recorded with a Horiba XploRa Raman spectrometer equipped with a 50 × long-range objective. The spectra were obtained using a 1200 lines per mm holographic grating with a circularly polarized laser of wavelength 532 nm, filtered at 10% of its maximum energy to avoid heating of the samples. Each spectrum presented in this work is an average of 5–7 spectra obtained on 5 to 7 different areas of each sample, and each of these 5–7 spectra is itself the result of the accumulation of 2 successive spectra acquired during 180 s on a range of Raman shifts between 200 and 3800 cm⁻¹.

2.3.3. Porosity and textural properties

The bulk density of the carbon architectures, ρ_b (g·cm⁻³), was obtained by the envelope method, using a Geopyc 1360 apparatus (Micromeritics, USA) and an ultrafine powder with a liquid-like behaviour (Dryflo®). During the measurement, the powder is forced to conform to the contours of a sample of known weight (without penetrating or compressing it) and allows a position sensor in the sample holder of calibrated volume to measure very precisely the volume occupied by the material, regardless of its geometry. The skeletal density, ρ_s (g·cm⁻³), was determined by helium pycnometry using an

automatic Accupyc II 1340 apparatus (Micromeritics, USA) by averaging 30 measurements. Prior to any measurement, the sample (first as a single piece to obtain the skeletal density, and then finely ground to obtain true density) was dried at 105 °C overnight. The total porosity ϕ (dimensionless) was then calculated according to Eq. (4):

$$\phi = 1 - \frac{\rho_b}{\rho_s} \quad \text{Eq. 4}$$

Mercury intrusion was performed on a piece of fractured material with an AutoPore IV 9500 apparatus (Micromeritics, USA) at two different pressure ranges, 0.001–0.24 MPa and 0.24–414 MPa. The inlet diameter D (m) of the pores, assumed to be cylindrical, was calculated by application of the Washburn equation (Eq. 5):

$$D = -\frac{4\gamma \cos \varphi}{P} \quad \text{Eq. 5}$$

where γ (0.485 J m⁻²) is the surface tension of mercury, φ (140°) is the contact angle between mercury and carbon, and P (Pa) is the intrusion pressure.

Adsorption experiments were carried out with Micromeritics ASAP 2020 and ASAP 2420 automatic adsorption apparatuses, using N₂ at –196 °C and CO₂ at 0 °C as molecular probes. Prior to analysis, samples (~1 g) were degassed under vacuum for at least 48 h at 110 °C. The Brunauer-Emmett-Teller [21,22] (BET) method was applied to N₂ isotherms to obtain the BET area, A_{BET} (m²·g⁻¹). The pore size distributions, the surface area S_{NLDFT} (m²·g⁻¹), and the total pore volume V_{tot} (cm³·g⁻¹), were determined by applying the 2D-NLDFT heterogeneous surface model available in the SAIEUS software (Micromeritics [23]) to the N₂ and CO₂ isotherms.

2.3.4. Mechanical properties

The mechanical properties of the carbons were obtained at a constant compression rate using a universal testing machine (Instron 4206) equipped with a 100 kN load cell. The samples were bounded to PMMA plates (6 mm thick) with a thin layer of epoxy glue and compressed along their direction of printing (*i.e.*, orthogonal to the successive layers). The deformation (mm) and the applied force (N) were recorded continuously until the samples broke. Strain (%) and stress (MPa) were obtained from the recorded data and the known dimensions of the samples. The Young's modulus was estimated from the slope of the stress-strain curves.

A Netzsch 402 F1 Hyperion® thermomechanical analyser (TMA) was used to evaluate the coefficient of thermal expansion of a sample based on its longitudinal dimensional changes between 20 and 900 °C at a heating rate of 10 °C·min⁻¹.

2.3.5. Electrical and thermal properties

Bulk electrical resistivity measurements were performed on 3D-printed rectangular samples (5 × 2 cm²) with a thickness of approximately 0.45 cm using the 4-point contact method according to ISO 3915. For in-plane measurements, silver paint was applied to both ends of the sample. Once the paint was dry, crocodile clips were applied to the silver paint-covered portion to apply an electric current using a Schuetz MR1012S digital ohmmeter. Two wedge-shaped electrodes (distance between wedge tips: 2 cm) were placed in the middle to measure the voltage drop using the same ohmmeter. The electrical resistivity was calculated according to Eq. (6):

$$\sigma = \frac{1}{R} \times \frac{L}{HW} \quad \text{Eq. 6}$$

where σ (S·cm⁻¹) is the electrical conductivity, R (Ω) is the resistance, L (cm) is the distance between the electrodes, and H (cm) and W (cm) are the thickness and the width of the sample, respectively.

For out-of-plane measurements, the configuration consisted of a planar stack composed of two metal plates as current electrodes, two

graphite sheets as intermediate contact layers, the sample sandwiched between the graphite sheets, and two thin gold wires (diameter 0.125 mm) as measurement electrodes positioned between the sample and the graphite sheets. A pressure of 3 N mm⁻² was applied to the stack to reduce contact resistances using a press. The electrical resistance was measured using again a Schuetz MR1012S digital ohmmeter, and the electrical conductivity was calculated according to Eq. (7):

$$\sigma = \frac{1}{R} \times \frac{t}{LW} \quad \text{Eq. 7}$$

where t (cm), L (cm) and W (cm) are the thickness, length and width of the sample, respectively.

Thermal conductivity measurements were performed in the out-of-plane direction at room temperature using a Netzsch LFA 447 laser flash diffusivity meter according to ASTM E146 on 3D-printed square samples (1 × 1 cm²) and thickness of approximately 0.2 cm. The specific heat was obtained with the same apparatus by comparison with a reference sample. Thermal conductivity was then calculated as the product of diffusivity, specific heat and density of the sample.

Both electrical and thermal conductivities were measured in an air-conditioned laboratory, *i.e.*, at 20 °C and 40% RH.

3. Results and discussion

In the following, the many techniques cited above were not applied to all samples. In particular, most chemical, textural and microstructural analyses have been carried out only on fragments of structure P, chosen arbitrarily for this purpose. Indeed, given that all samples were prepared from the same precursors, used in the same proportions and under the same processing conditions, we can therefore safely claim that the type of carbon obtained, or more precisely the type of carbon-carbon composite obtained, is rigorously the same for the 3 types of architectures produced. Actually, these are microscopic characteristics, and there is no doubt that 3D design and macroscopic porosity have absolutely no effect on them, and we have pointed out (see again Fig. 2) that cell size and, above all, wall thickness, are identical from one structure to the other. Consequently, if the composition of the carbon precursors were the same, and if the mass transfer conditions at cell scale during infiltration and pyrolysis were the same too, it seems pointless to verify that the porosity, composition and internal microstructure of the constituent carbon are the same from one architecture to another. Nevertheless, we were keen to check that the intrinsic porosity, whether open or closed, was the same in each structure. The same reasoning applies to oxidation behavior, which in this case might have depended on the 3D architecture due to different mass and heat transfers under high-temperature air flow at the macroscale, using such dynamic conditions, but which was tested on small fragments of structure P. This way of doing is therefore indicative of the intrinsic behavior of the constituent carbon since no remnants of the original architecture are left. On the other hand, mechanical properties, which are highly dependent on geometric porosity and 3D architecture, have been well studied for all materials.

3.1. Material processing and densification

3D printing of TPMS structures was used to fabricate green cylindrical parts composed of graphite-carbon black powders and phenolic matrix. Their diameter, height and TPMS thickness were 21.75 ± 0.03 mm, 37.74 ± 0.05 mm and 0.85 ± 0.02 mm, respectively. The complex geometry of the architecture was reproduced with satisfactory precision compared to the computational models. Infiltration and subsequent pyrolysis of the parts produced graphite-amorphous carbon composites with low shape distortion and very few macroscopic cracks. The final pyrolyzed samples had a diameter of 19.44 ± 0.05 mm, a height of 33.68 ± 0.07 mm, and a TPMS thickness of 0.76 ± 0.04 mm. Despite a linear

shrinkage of $10.5 \pm 0.3\%$, the parts retained their shape, as it can be seen in Fig. 3a. Fig. 3b displays the evolution of the mass of the cellular structures during the different stages of their manufacturing process.

The carbon yield of the furan resin at 1000°C was found to be 52% , and the bulk density of the as-obtained amorphous carbon was 1.921 g cm^{-3} . The volume fraction of amorphous carbon formed during pyrolysis of the furan resin was estimated to be 24.6% using Eq. (8).

$$\text{Amorphous } C_{\text{vol.\%}} = \frac{\frac{(M_{\text{inf}} - M_{\text{print}}) \cdot y_{\text{fur}}}{\rho_{\text{amorphous } C}}}{\frac{(M_{\text{inf}} - M_{\text{print}}) \cdot y_{\text{fur}}}{\rho_{\text{amorphous } C}} + \frac{M_{\text{print}}}{\rho_{\text{graphite-CB}}}} \quad \text{Eq. 8}$$

where M_{inf} is the mass of the sample after infiltration, M_{print} is the mass of the sample after 3D printing, y_{fur} is the carbon yield of the furan resin after pyrolysis, $\rho_{\text{amorphous } C}$ is the true density of the amorphous carbon, and $\rho_{\text{graphite-CB}}$ is the true density of the graphite-CB mixture. The remaining 75.4% of the volume consists of 2.0% of amorphous carbon derived from the pyrolysis of the phenol in the binder, a value arrived at by the authors based on their prior research and expertise, 69.7% of graphite, and 3.7% of carbon black powder. Therefore, the total amount of non-graphitic carbon phase was estimated to be $30.3\text{ vol}\%$.

3.2. Microstructure

A sample of Primitive (P) structure (see again Fig. 1) was observed by SEM at the level of its natural surface after synthesis, but also after deliberately breaking off a piece to observe details of the fracture surface. Representative images are shown in Fig. 4. It can be clearly seen that the natural surface of the material is granular, with grains of relatively well homogenous size between 10 and $20\ \mu\text{m}$, which corresponds to the grain size of the graphite used (Fig. 4a and b). These grains appear to be embedded in a carbon matrix that perfectly encapsulates them,

giving them a very rounded and blunt contour. At higher magnification, it can also be seen that the surface of this matrix is covered with microspheres of approximately $200\text{--}300\text{ nm}$ in diameter (Fig. 4c), which are probably the remains of a slight demixing in the resin coating the graphite grains and having led to a molten phase prior to conversion into carbon during pyrolysis.

The fractured surface clearly reveals the composite nature of the material, as the surface is pitted with craters corresponding to the pulling out of the graphite grains (Fig. 4d). The fracture is clearly adhesive, and not cohesive, as no broken graphite grains could be observed, only the detachment of the grains from their carbon matrix (Fig. 4e). We are therefore dealing here with a graphite-carbon composite, in the sense that the carbon used as matrix is not of the same nature as that used as filler. The analyses below confirm the highly disordered nature of the carbon derived from phenolic/furanic resin, whereas graphite is a well-crystallized material.

On a more macroscopic scale, X-ray tomography enables three-dimensional images to be reconstructed very efficiently from the thin slices acquired by the apparatus, as shown in Fig. 5. The tomography thus highlights the adequate resolution with which the samples could be printed (Fig. 5a–d). The examination of the structure on a smaller scale shows a fine porosity with a circular aspect in the sectional planes (Fig. 5e). A short video is given in the Electronic Supplementary Information, showing what is seen by travelling through the sample along the printing axis, thus in the direction perpendicular to the successively deposited layers. It allows seeing that these pores are not channels that would communicate from one layer to another, but are globally spherical, with diameter between 60 and $120\ \mu\text{m}$. They are thus bubbles that must have been formed by gas release during pyrolysis, and their spherical shape confirms the hypothesis of the appearance of a transient liquid phase during the thermal treatment. These bubbles, except in the case where gas was trapped in the structure of the material, must thus

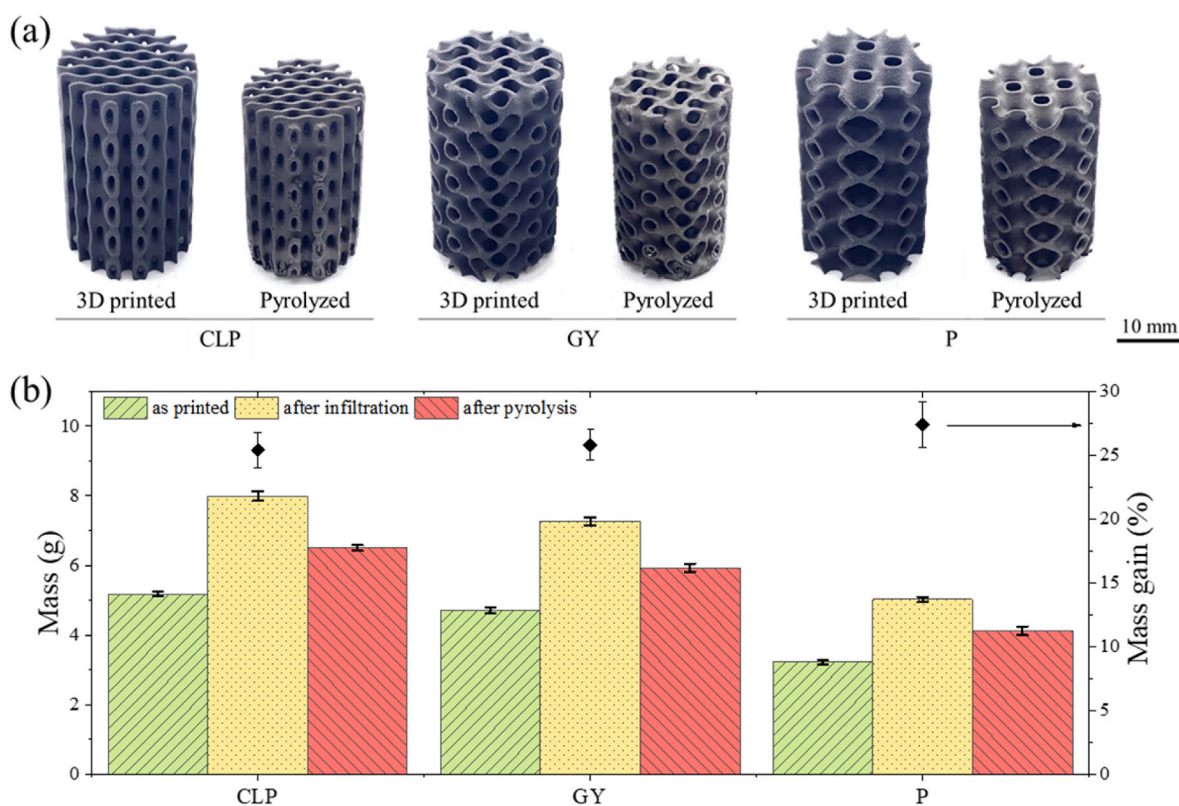


Fig. 3. (a) Optical images of the three cellular structures after 3D printing and pyrolysis; (b) Measured mass of the sample during the different stages of the manufacturing process, the mass gain being calculated with respect to the original 3D structure. (A colour version of this figure can be viewed online.)

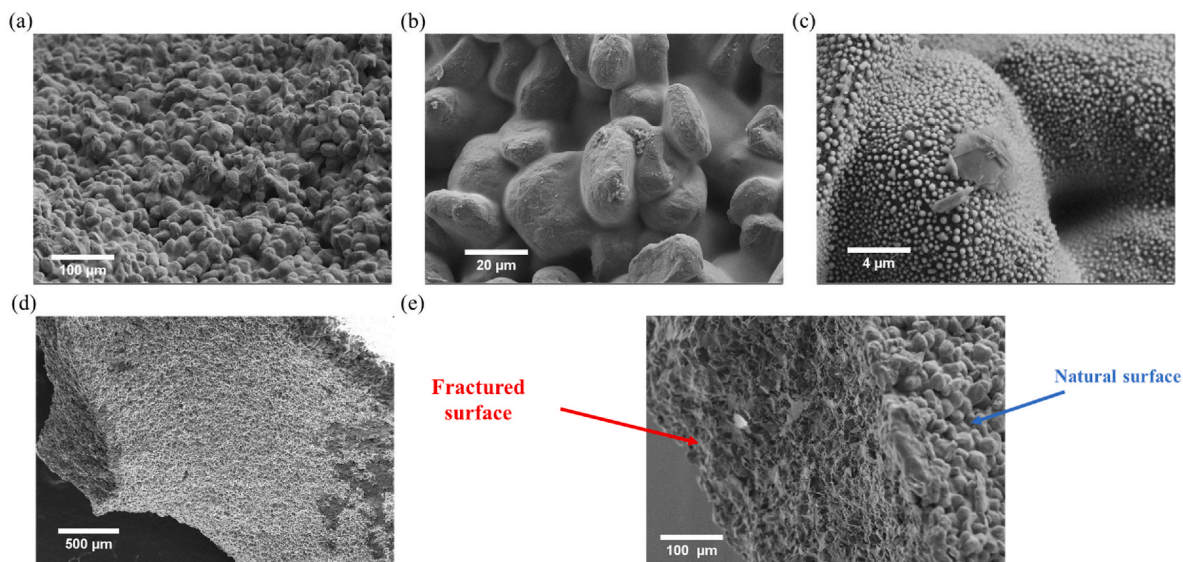


Fig. 4. SEM images at different magnifications: (a)–(c) of the natural material surface; and (d)–(e) of the surface after fracture. (A colour version of this figure can be viewed online.)

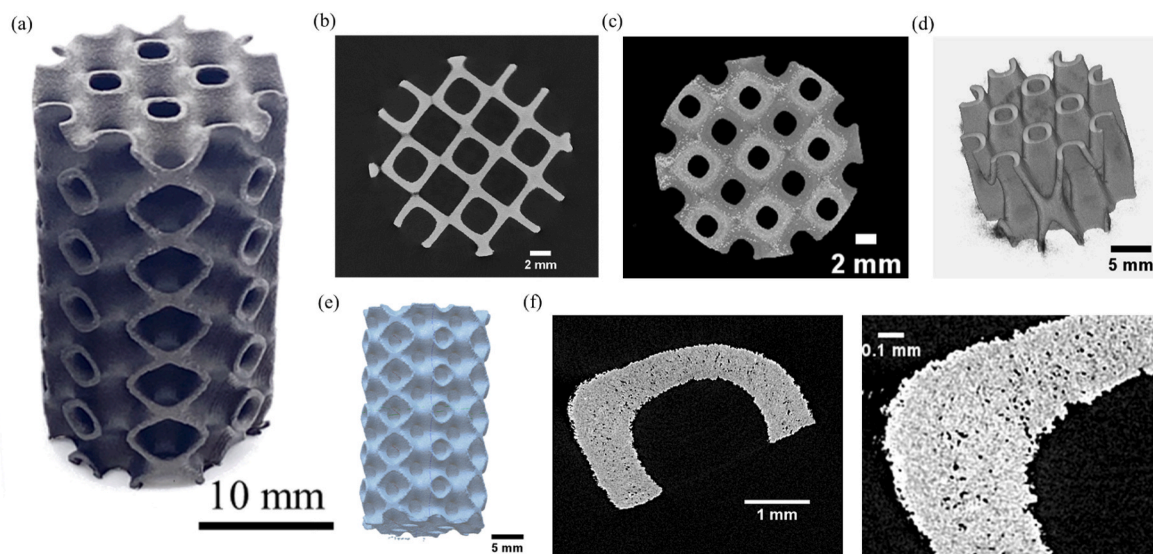


Fig. 5. X-ray tomography images of (a) sample P showing: (b) a slice; (c) the total volume projection; (d) a partial volume reconstruction; (e) the total volume reconstruction; and (f) the detail of the internal porosity at two different magnifications. (A colour version of this figure can be viewed online.)

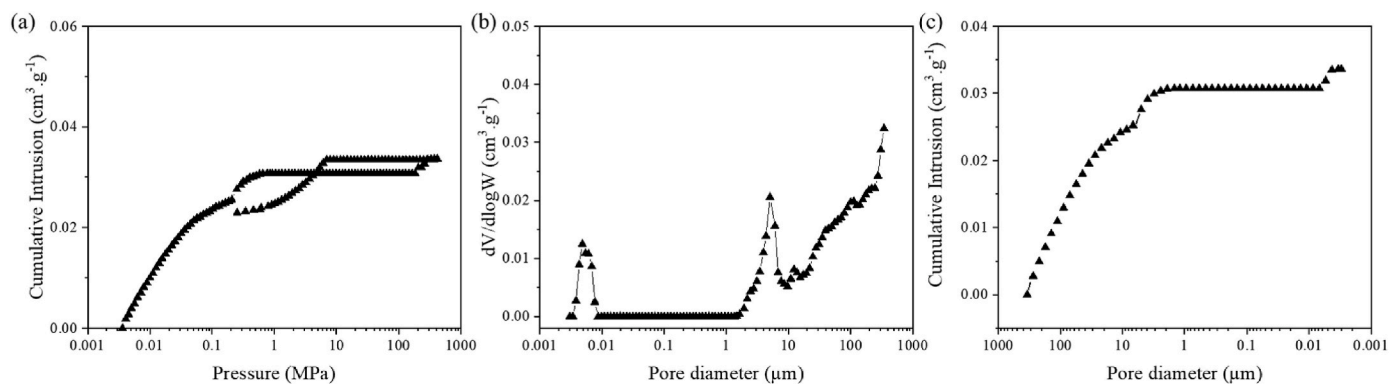


Fig. 6. Mercury intrusion porosimetry results: (a) raw intrusion-extrusion curves; (b) pore size distribution; and (c) cumulative volume as a function of pore size. (A colour version of this figure can be viewed online.)

communicate with the external surface through narrow cracks, which the resolution of the tomograph used does not allow visualizing.

This particular shape of the pores is confirmed by mercury porosimetry (Fig. 6). This technique applies mercury to the sample at increasing pressure and at the same time measures the amount that was able to penetrate (Fig. 6a). Once the maximum pressure is reached, in this case a little over 400 MPa, the pressure is relaxed to allow the mercury to extrude, which provides information about the connectivity of the pores [24]. Fig. 6a clearly shows that mercury penetrates continuously from low pressures until it reaches a plateau at which the material appears to be saturated. Only at very high pressures, just before the limit of the device, a small amount of mercury can be introduced again. When the pressure drops, this mercury is not extruded immediately: it remains trapped over a wide range of pressures, indicating "ink bottle" pores, (i.e., with a body of larger diameter than the neck that gives access to it). It is only below 10 MPa that the mercury finally exits suddenly to return to a volume at about the same level as at intrusion. We can therefore deduce that the smallest pores communicate with some larger cavities that are only accessible through them [25]. However, the largest pores, more likely cracks in view of the corresponding calculated diameters, communicate with each other up to the intrusion plateau.

The corresponding pore size distribution (PSD) is shown in Fig. 6b. The PSD is rather multimodal, indicating the presence of a broad range of pore diameters (W). Two peaks in the distribution are particularly visible between 1 and 10 μm on the one hand, and around 5 nm on the other, but the PSD also contains a large number of pores with a diameter between 10 and 350 μm . The median pore size of the material was estimated to be about 52 μm , a value that is in the same order of magnitude as what was observed by tomography. By deliberately plotting the PSD as $dV/d\log W$ versus W , the population of pores narrower than 0.01 mm is well highlighted, but the latter should not be overestimated either. Fig. 6c thus shows the cumulative pore volume as a function of W , revealing that pores smaller than 0.01 nm in diameter contribute only 9% of the total pore volume. In contrast, pores with diameters between 1 and 10 μm account for 19% of the total pore volume, while those with diameters between 10 and 350 μm account for 72% of the total pore volume.

The mercury intrusion method has, nevertheless, several limitations. One is that it cannot intrude mercury at pressures greater than 400 MPa, which does not reveal pores narrower than 3.7 nm, according to Eq. (9). The other is that only open porosity can be detected. For this reason, gas adsorption experiments were performed, on the one hand with N_2 as probe molecule at -196°C to apply the well-known BET method for specific surface area measurement, and on the other hand with CO_2 at 0°C to probe pores smaller than 0.7 nm. In both cases, negligible uptakes were measured (thus not shown), i.e., within the experimental error of the technique. We can therefore safely conclude that the specific surface area is close to $0\text{ m}^2\text{ g}^{-1}$, and that the corresponding pore volumes are also zero. The latter should not be confused with the macroscopic porosity ($>50\text{ nm}$), in which gas adsorption is negligibly small. As seen by tomography and mercury intrusion, the material is porous at the macroscale, and this porosity can be calculated in two ways.

One method of determining porosity is to measure the envelope density, for example by powder pycnometry as we have done, giving the value of ρ_b on the one hand, and to measure the skeletal density by helium pycnometry, giving the value of ρ_s on the other. The total porosity is then calculated by Eq. (4), and the result depends on whether the sample has been previously ground into a fine powder or not. Without grinding, the porosity is 8%, after grinding it is about 20%. A significant fraction of the sample volume, about 12%, therefore consists of closed porosity. The corresponding values are shown in Table S2. It should be noted that the skeletal density after grinding, slightly higher than 2 g cm^{-3} , is closer to what could be expected for a carbonaceous material rich in graphite, the density of which being about 2.2 g cm^{-3} . These values confirm the presence of closed porosity in the non-ground

material.

The second method of measuring porosity is to measure the amount of mercury intruded per gram of material at the highest pressure accessible by this technique (see again Fig. 6). In this case, the porosity Φ is calculated by applying Eq. (9):

$$\Phi = \rho_b V_{sp} \quad \text{Eq. 9}$$

where V_{sp} ($\text{cm}^3\cdot\text{g}^{-1}$) is the specific pore volume measured at the high-pressure intrusion plateau. In this case, the calculated porosity is 6.2%. Even if this value is well within the order of magnitude of what had been evaluated through Eq. (4), it is still about half of it. However, if the narrowest pores are inaccessible to mercury, which reduces the estimated porosity value, it is not excluded that the powder pycnometry used to evaluate the bulk density also has its own limitations. Indeed, the displacement medium used is the commercial material known as Dry-Flo®, whose peak particle diameter is slightly higher than 100 μm , with particles up to 200 μm , and with proven cases of agglomerates of size sometimes exceeding 1 mm [26]. When we look again at Fig. 5, showing channels of about 2 mm in diameter, we can legitimately think that the open porosity of the monoliths is incompletely filled by this powder, and that the bulk density has been underestimated. This amounts to saying that the porosity calculated by Eq. (4) is overestimated. The open porosity of these 3D printed carbons should therefore probably be between the values determined by the two techniques, i.e., between 6 and 12%.

3.3. Composition and texture

The results of elemental analysis are as follows, expressed in wt. %: carbon 98.44; hydrogen 0.29; nitrogen 0.33; sulfur 0.00; and oxygen 0.94. As expected, the carbon content is almost 100%, in agreement with the high graphite content constituting the material. The oxygen content of about 1%, and the presence of hydrogen and nitrogen as impurities, are attributable to the carbon derived from the resin used as a binder. It is indeed well known that, even after treatment at very high temperature, oxygen is never completely eliminated from this type of carbon, often called vitreous carbon. It is indeed an isotropic carbon, rather brittle, with conchoidal fracture, hard and smooth, very different from graphite, which is anisotropic, easy to cleave, and soft from the mechanical point of view.

X-ray diffraction confirms the coexistence of two main phases in the material, one well crystallized, the other extremely disordered. The XRD pattern shown in Fig. 7a clearly shows very thin bands due to the graphite, as well as a diffusion background superimposed on it. Using Eva software, and estimating that the background noise corresponds to the amorphous phase, we calculated that 71.5% of the material volume is crystalline, while the volume fraction of carbon serving as a binder between the graphite grains represents 28.5%. These proportions are necessarily approximate, given the method of calculation, but are still in excellent agreement with the initial formulation (see again section 3.1, where it has been shown that about 70% of the volume of the material is graphite). Then, using TOPAS software (Total Pattern Analysis Solution, supplied by Bruker), the diffraction pattern was fitted for the hexagonal and rhombohedral phases over the whole diagram (not shown), giving respective proportions of 66 vol% and 34 vol% for these two phases. It is thus a defect-rich graphite, probably due to an intense mechanical treatment to shape it into very rounded grains, known to lead to the formation of a very significant proportion of rhombohedral phase. Using the same software, and based on the 100 reflection, the size of the coherent domains, L_a , was found to be 25 nm. The analysis of Fig. 7a finally allowed to determine the interplanar distances for the two phases, and which are $d_{002} = 3.355\text{ \AA}$ for the hexagonal phase, and $d_{003} = 3.356\text{ \AA}$ for the rhombohedral phase, in very good agreement with the usual values for a graphite.

X-ray diffraction is a global method, giving a diffraction pattern that

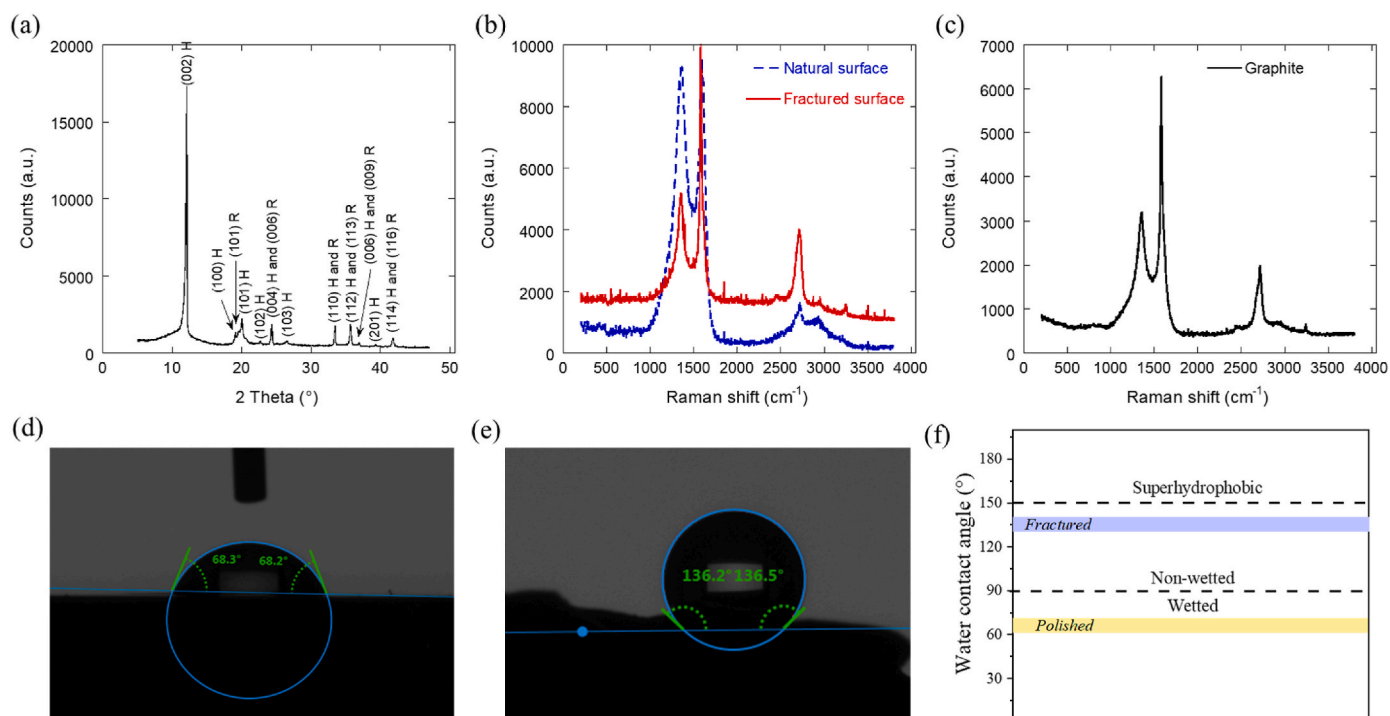


Fig. 7. (a) XRD pattern of the material, obtained at a wavelength of 0.70930 \AA , with peak indices referring either to the hexagonal structure (H) or to the rhombohedral structure (R) of graphite. Raman spectra of: (b) the surface of the 3D-printed material, natural and after fracturing, and (c) the graphite used in the formulation. Water contact angle measured on: (d) polished material, and (e) fractured material. (f) Wetting properties of the binder-jetted carbon. (A colour version of this figure can be viewed online.)

is only a weighted average of the different phases present. On the other hand, Raman micro-spectrometry (Fig. 7b) is a local method that allows information to be obtained on specific zones of a given sample. It was thus possible to distinguish between the natural surface of the sample and the fractured surface. The former surface (see again Fig. 4e) indeed exhibits graphite grains completely covered with ex-resin carbon, thus a very disordered carbon, while the latter surface allows graphite grains to protrude, without however being able to observe graphite alone by Raman, the size of the laser spot being larger than that of an individual graphite grain. Fig. 7b nevertheless shows unambiguously that the material seen on a fractured surface is clearly more ordered than that seen on the natural surface. Indeed, the D and G bands, respectively at about 1350 and 1580 cm^{-1} , attributed to defects within the carbon layers and to heteroatoms for D, and to the C–C elongation mode in the aromatic rings for G [27], have very different intensity ratios. These two bands are much narrower on the fractured surface, with a FWHM of about 89 and 38 cm^{-1} for D and G band, respectively, against 193 and 119 cm^{-1} , respectively, for the natural surface. Their D/G intensity ratio is also significantly lower (0.52 , instead of 0.99 for the natural surface), and this indicates that the material seen by the laser is considerably more graphitic.

The second order spectrum (typically between 2300 and 3300 cm^{-1}) is also interesting insofar as its structuring is different, depending on whether one looks at the natural or fractured surface, a sign that the disorder is not the same in the stacking of the carbon layers. It may be useful to recall here that the 1st order and the 2nd order give information on the structural disorder in the carbon layers, and on the stacking order perpendicularly to them, respectively [28]. The band around 2710 cm^{-1} , called 2D because attributed to the first overtone of the D band [29,30], is the most developed and is always present in the Raman spectra of highly ordered graphites. We can also see a bump around 2940 cm^{-1} , called G + D because attributed to the combination of the G and D modes [29,30]. The 2D band is much more intense and the D + G band better resolved on the fractured surface, a further evidence of a

better structural order in the direction of the stacking of the carbon sheets due to the presence of graphite grains directly visible by the laser.

These arguments are corroborated by the examination of the Raman spectra of the graphite used as filler in the formulation. Fig. 7c shows that the corresponding spectrum is much more similar to that of the fractured surface of the material, where the graphite is exposed but not alone, than to that of the natural surface where the graphite is under a very covering layer of highly disordered resin-derived carbon. Not only is the general profile the same, with very close D/G intensity ratios, but we can also see that the band around 2430 cm^{-1} is also better resolved; this band is usual at 2nd order, in addition to the two other bands already discussed above, in highly graphitic materials with the best 3D structural order [31]. The size of the coherent domains, L_a (nm), could be calculated from the equation of Caçado et al. [32], known to apply to graphitic materials:

$$L_a = \frac{560}{E_L^4} \left(\frac{I_D}{I_G} \right)^{-1} \quad \text{Eq. 10}$$

where E_L (eV) is the energy of the laser line (here 2.33 eV at 532 nm), and I_D and I_G are the intensities of D and G bands, respectively. The data in Fig. 7c led to a value of $L_a \approx 37 \text{ nm}$, which confirms the graphitic character of the material and, at the same time, that a significant amount of defects is present, limiting the spatial extent of its crystallites, in agreement with the non-negligible intensity of the D band. This value is higher than that, 25 nm , found by XRD, but on the one hand, Eq. (10) is approximate, and on the other hand, the XRD was done on a volume of material containing also disordered ex-resin carbon; it is therefore not surprising that the value found by Raman on pure graphite is higher.

Because of its composition and the nature of its constituents, one would not expect this 3D-printed material to be particularly hydrophilic. Carbon is indeed considered a hydrophobic material [33], but graphite itself is much less hydrophobic than is usually thought [34]. Carbon can even become quite hydrophilic when its surface is rich in oxygenated groups [35]. In the present case, taking into account the presence of

oxygen in the carbon used as a binder between the graphite grains and its non-crystalline nature, the contact angle measured with water on a polished surface is about 68° (see Fig. 7d), thus well below the 90° limit beyond which the material is considered as non-wetting. In contrast, after fracturing, the surface becomes significantly less wettable by water, with the contact angle becoming slightly greater than 136° (Fig. 7e).

This is a considerable change, although it is insufficient to consider the material superhydrophobic; this would have required the contact angle to become greater than the commonly accepted value of 150° [36] (Fig. 7f). This sudden increase in the contact angle is not due to the presence of graphite grains on the surface, since graphite was already apparent after polishing the surface, but to the roughness of the surface thus generated. It is indeed well known (for examples and details, see for instance Ref. [37] and refs. therein) that a very rough surface can, at constant composition, become hydrophobic by lotus effect or by rose effect. In this case, however, it is impossible to attribute quantitatively which part of the surface chemistry and which part of the roughness leads to this doubling of the water contact angle. It is all the more difficult to distinguish between the effects of chemistry and roughness, as polishing is known to introduce defects in graphite [38] and help chemisorption of water on it [39], a phenomenon by which it can become more hydrophilic.

3.4. Mechanical properties

Fig. 8a shows three representative stress-strain curves, each of which obtained for a different apparent density of the 3D-printed materials.

The mechanical characteristics of each sample are grouped in Table S3 and can also be seen in Fig. 8c. As expected, the Young's modulus, ranging from 312 to 1235 MPa, the compressive strength, with values from 2.01 to 24.10 MPa, as well as the strain at break (from 0.93 to 2.65%), increase dramatically with the bulk density of the materials. It can also be observed that the fractured samples, shown in Fig. 8b, exhibit clean fractured facies, as the samples were clearly sheared along their diagonal. This is in good agreement with the brittle fracture observed in Fig. 8a, according to which the sample does not collapse gradually with increasing stress, but breaks abruptly. This mode of fracture, which is the only one to enable a correct determination of both the modulus and the fracture resistance, was obtained thanks to the preliminary bonding of rigid plates to the opposite faces of each binder-jetted sample (i.e. GY, CLP and P structures), which allowed an excellent distribution of the forces on the material [40,41].

The mechanical properties of CLP and GY samples were found to be superior to those of compressed carbon-graphite composite (obtained by phenolic resin impregnation) with compressive strength ranging from 7 to 19.7 MPa at a density of 1.2 g cm^{-3} [42]. In the context of 3D-printed carbon, CLP and GY (0.69 and 0.61 g cm^{-3} , respectively) samples showed higher range of mechanical properties than porous carbon of similar density (about 0.55 g cm^{-3}) obtained by direct ink writing with compressive strength and Young's modulus values of 5.1 and 243 MPa, respectively [43]. P sample, which is lighter than its counterparts (with an apparent density of 0.41 g cm^{-3}), showed similar mechanical properties to those of carbon obtained by stereolithography of bio-based precursors with a density of between 0.39 and 0.47 g cm^{-3} [44,45]. Note that the CLP, GY and P structures had geometric porosities of

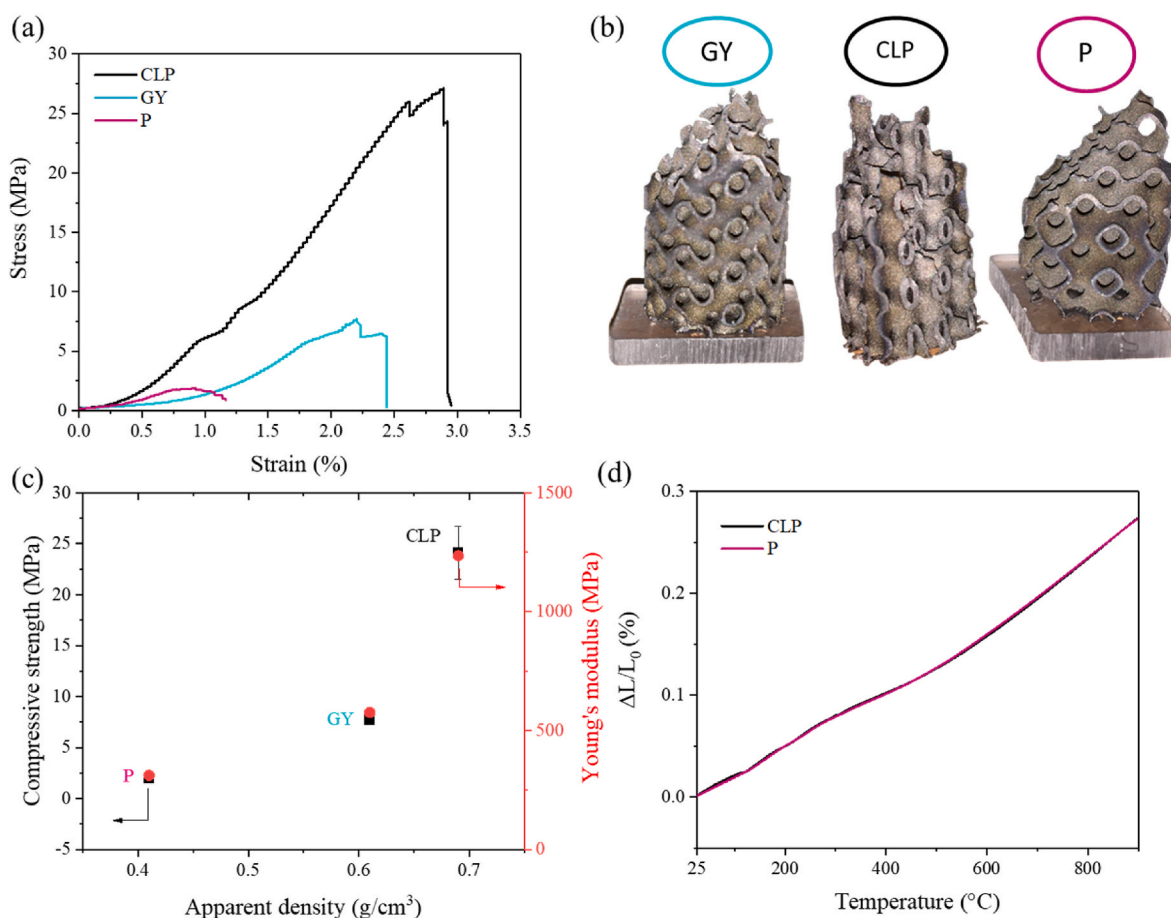


Fig. 8. (a) Stress-strain curves of samples of 3 different bulk densities, subjected to uniaxial compression; and (b) photos of the binder-jetted samples after the mechanical tests; (c) average compressive strength and Young's modulus as a function of the apparent density of the 3D architectures (most error bars are smaller than experimental points). (d) Dilatometry curve of CLP and P samples. (A colour version of this figure can be viewed online.)

61.9%, 67.0% and 75.6%, respectively. This indicates that the mechanical strength of the skeleton material must be significantly greater.

The expansion curve of a sample, measured by TMA, is given in Fig. 8d. It can be seen that the expansion is roughly linear up to 550 °C, above which temperature a slight change in slope occurs. The curve can therefore be considered as a succession of two segments whose slopes represent the expansion coefficients, equal to $2.7 \times 10^{-6} \text{ K}^{-1}$ and $3.8 \times 10^{-6} \text{ K}^{-1}$ below and above 550 °C, respectively. These values are of the same order of magnitude as those given in the literature for various graphites, namely $3.3 \times 10^{-6} \text{ K}^{-1}$ for extruded graphite, $4\text{--}6.4 \times 10^{-6} \text{ K}^{-1}$ for isotactic graphite [46], and $2.7 \times 10^{-6} \text{ K}^{-1}$ for artificial graphite [47]. These values can also be compared with those of glassy carbon obtained by pyrolysis at very high temperature of polyfurfuryl alcohol: $3.5 \times 10^{-6} \text{ K}^{-1}$ for Sigradur K from HTW, carbonized at 1000 °C [48], and $3.49 \times 10^{-6} \text{ K}^{-1}$ for glassy carbon in general [49]. The reticulated vitreous carbon foams marketed by ERG have an average expansion coefficient of $3.2 \times 10^{-6} \text{ K}^{-1}$ [50]. The measured values are thus typical of artificial graphite on the room temperature side, and of those of glassy carbon at higher temperatures.

3.5. Oxidation behavior

The curve of mass change of sample P subjected to a temperature increase of $15 \text{ °C}\cdot\text{min}^{-1}$ under synthetic air with a flow rate of 50 mL min^{-1} is shown in Fig. 9a. In the same plot, the differential expressed as % mass loss per min is also shown. It can be seen that the mass is unchanged up to 500 °C, which is remarkable under oxidizing conditions like these. Above this temperature, the sample gradually gasifies and reaches a peak oxidation rate at about 915 °C. It should be noted that, on the differential curve, there is a very clear change of slope at the temperature of about 635 °C, highlighting a rapid loss of mass between 500 °C and 635 °C and a much slower loss of mass beyond. This obviously corresponds to the preferential oxidation of the disordered carbon covering the graphite grains, followed by the much more difficult oxidation of the graphite on the higher temperature side. Under the conditions of this test, the sample was completely consumed at about 1100 °C, a temperature beyond which the mass loss was 97%.

The relative mass loss as a function of oxidation time for the binder-jetted carbon-graphite composite P at temperatures between 500 and 700 °C is shown in Fig. 9b. As can be seen, the oxidation rate increases significantly with temperature, as long as the latter is below 650 °C. By further increasing the oxidation temperature, the oxidation rates remained almost constant, suggesting a change in the mechanism controlling oxidation. Since, under the measurement conditions, oxidation resistance is dominated by textural properties, similar curves (not shown here) are obtained for CLP and GY samples.

The Arrhenius plot of the carbon-graphite binder-jetted composite in

the temperature range 500 °C–700 °C is shown in Fig. 9c. The plot is linear between 500 and 650 °C, and then a break in slope can be observed between 650 and 700 °C. The decrease in apparent activation energy tends to confirm that the oxidation mechanism has shifted from a kinetic control (regime I, between 500 and 650 °C) to a pore-diffusion control mechanism (regime II, >650 °C). This regime change temperature, although dependent on the oxygen flow [51], remains in the same order of magnitude as the regime change observed for graphite and carbon-carbon composites (*i.e.*, between 600 and 750 °C) [20].

The activation energy measured between 5 and 10% mass loss, with a low value of 87 kJ mol^{-1} , can be associated with the preferential oxidation of the amorphous carbon (with a relatively low specific surface area) surrounding the graphite grains and might suggest the presence of impurities in the graphite [52]. Indeed, the activation energies for the majority of graphite materials are generally reported between 168 and 210 kJ mol^{-1} in regime I [20,53], and the presence of impurities or non-graphite binder tends to decrease the activation energy of the oxidation reaction. Moreover, values between 38 and 76 kJ mol^{-1} have been reported for 3D-printed carbons prepared from non-graphitizable precursors, known to give amorphous carbon upon pyrolysis [54]. It is thus normal, for an amorphous carbon-graphite composite such as the one studied here, to find activation energies intermediate between those of pure graphite and pure amorphous carbon.

3.6. Electrical and thermal conductivity

The measured values of in-plane and out-of-plane electrical conductivity were found to be equal to $351 \pm 6 \text{ S cm}^{-1}$ and $99.5 \pm 5.5 \text{ S cm}^{-1}$, respectively. The higher conductivity along the printed layers suggests that the graphite grains were not perfectly round but rather oblate ellipsoids as is most often the case [55], and that a preferential orientation of these ellipsoids took place during the preparation of the materials. Since graphite is a highly anisotropic lamellar solid, with an electrical conductivity typically 1000 times higher parallel to the atomic carbon sheets than perpendicular [56], it is not surprising to find a higher conductivity along the printed layers. However, this anisotropy is obviously not as pronounced as for natural graphite, for several reasons: (i) artificial, polycrystalline graphite grains, thus with more defects, have been used; (ii) their orientation is not perfect because these are not platelets that would lie flat on a plane substrate (see again Fig. 4b, evidencing ellipsoidal grains with an aspect ratio between approximately 2 and 3); (iii) the amorphous carbon that acts as a binder between the graphite grains further reduces the macroscopic anisotropy. It can even be argued that, even if the graphite grains were not intrinsically anisotropic, the preparation method would probably have induced anisotropy in the properties, as is most often the case with layer-by-layer 3D printing. Indeed, it is well known that 3D-printed structures tend to

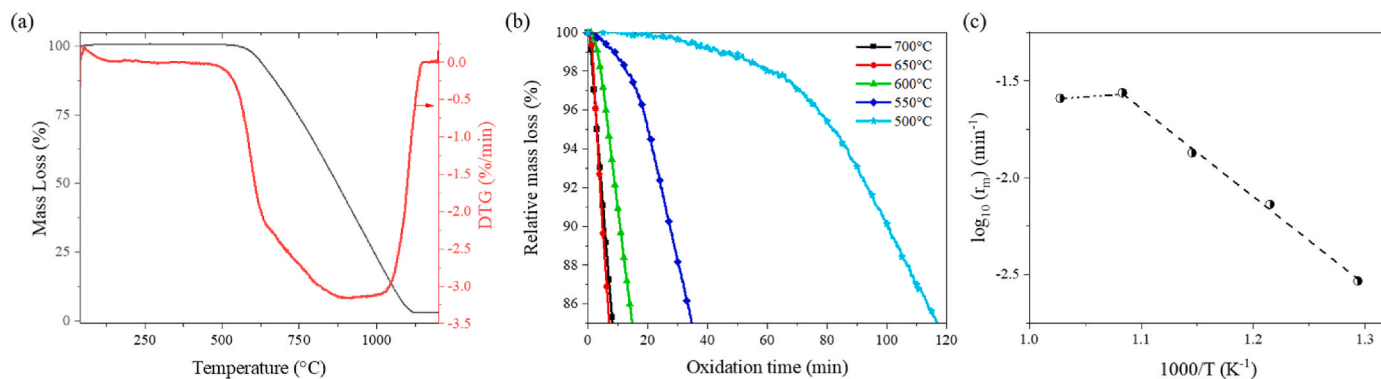


Fig. 9. (a) Thermogravimetric analysis of binder-jetted carbon sample P heated at 15 °C min^{-1} under synthetic air flow: mass loss (black curve) and differential (red curve); (b) Mass loss as a function of oxidation time at different temperatures between 500 and 700 °C; and (c) the corresponding Arrhenius plot. (A colour version of this figure can be viewed online.)

exhibit conductive anisotropy (by electrons and phonons) due to the existence of contact resistances between the layers, which reduce both electrical and thermal conductivity.

It is possible to try to find the conductivity value of the non-porous carbon skeleton from the measured values, considering that the 3D printed composite block has an intrinsic porosity of 20% (see again Table S2). For this purpose, we use the following equation, which is a good approximation for rigid open-cell foams with node effects [57,58]:

$$\sigma_s = \frac{3\sigma}{(1-\phi) + 2(1-\phi)^{3/2}} \quad \text{Eq. 11}$$

where σ_s is the electrical conductivity of the conductive skeleton, σ that of the porous composite, and $\phi = 0.2$ its porosity. With a measured value $\sigma = 351 \text{ S cm}^{-1}$ in the planar direction, we find by application of Eq. (11) that $\sigma_s = 527 \text{ S cm}^{-1}$.

The latter value can be compared with what can be calculated for a biphasic mixture of amorphous carbon and graphite using the effective medium theory, and more specifically Bruggeman's asymmetric model, since we are dealing here with a phase of amorphous carbon that surrounds the graphite grains. The effective conductivity σ_e of the medium then verifies the following equation [59]:

$$0.7 \frac{\sigma_1 - \sigma_e}{\sigma_1 + 2\sigma_e} + 0.3 \frac{\sigma_2 - \sigma_e}{\sigma_2 + 2\sigma_e} = 0 \quad \text{Eq. 12}$$

where 0.7 and 0.3 are the volume fractions of graphite and amorphous carbon, respectively, and σ_1 and σ_2 are the electrical conductivities of graphite and amorphous carbon, respectively. This equation can be solved analytically and has two solutions such as:

$$\sigma_e \rightarrow \frac{1}{4} \left(-\sigma_1 + 3 \times 0.7 \sigma_1 + 2\sigma_2 - 3 \times 0.7 \sigma_2 \pm \sqrt{8\sigma_1\sigma_2 + (-\sigma_1 + 3 \times 0.7 \sigma_1 + 2\sigma_2 - 3 \times 0.7 \sigma_2)^2} \right) \quad \text{Eq. 13}$$

the one with a physical meaning being the one with a positive value.

Eq. (12) is valid for spherical inclusions, whereas we know that graphite is in the form of ellipsoids with an aspect ratio of around 2 to 3. More complex models exist that consider ellipsoidal inclusions, but we have chosen not to take them into account, given the large uncertainties on the bulk conductivity values of the phases present, which we ignore in the present case and have searched for in the literature. Thus, using average electrical conductivity values of 850 S cm^{-1} for isostatic graphite [60] and 40 S cm^{-1} for amorphous carbon [61,62], we find an effective electrical conductivity value of 500 S cm^{-1} for the non-porous carbon-carbon composite. Given the approximations made to arrive at this result, we can consider that it is in surprisingly good agreement with the value estimated through Eq. (11).

Regarding the specific heat, necessary for the calculation of the thermal conductivity through a measurement of thermal diffusivity, a value of $0.725 \pm 0.035 \text{ J g}^{-1} \text{ K}^{-1}$ has been found. This value is quite close to what was expected for graphite, $0.705 \text{ J g}^{-1} \text{ K}^{-1}$ [63], but also for amorphous carbon [64], as at room temperature this quantity is very little sensitive to the structural order of sp^2 carbon. The measured out-of-plane diffusivity, equal to $(1.023 \pm 0.082) \times 10^{-5} \text{ m}^2 \text{ s}^{-1}$ and comparable to that of cast iron, carbon steels and technical ceramics such as Si_3N_4 [65], then allowed to calculate an out-of-plane conductivity of $12.05 \pm 0.35 \text{ W m}^{-1} \text{ K}^{-1}$. This value is lower than that of polycrystalline graphites, $160\text{--}200 \text{ W m}^{-1} \text{ K}^{-1}$ [66] but, as was also true for the electrical conductivity, it must be taken into account that: (i) the material is intrinsically porous to the extent of about 20% on the one hand; (ii) the measurement was carried out in the less conductive direction; (iii) the graphite grains do not percolate into the composite material (as demonstrated by the non-conductive nature of the

composite just after 3D printing, i.e. before infiltration and pyrolysis) but are embedded in an amorphous carbon matrix. The value found is nevertheless higher than that of non-porous amorphous carbon derived from furan resin ($3.5 \text{ W m}^{-1} \text{ K}^{-1}$ [67]).

The present 3D-printed carbons, in consideration of their electrical conductivity and their resistance to oxidation in air at high temperature, could be used as Joule heating elements. Indeed, the conductivity is in the range of what has been reported for some composites based on CNTs dispersed in PAN [68], and which heat up very strongly when traversed by a current of a few mA. This heating strongly modifies the composite, which can be an advantage to modify its conductive properties at will, but gives a material with non-stabilized properties due to the progressive modification of the polymer matrix. Nothing like this is supposed to happen with a carbon-carbon composite as in the present case.

Regarding the thermal conductivity, it is interesting to verify if the measured value is in the range of what has been recently proposed for porous carbons hosting phase change materials for seasonal thermal storage [69]. This type of energy storage requires highly porous structures to encapsulate a maximum amount of phase change material but, in order to cover the power needs in a wide range of seasonal storage applications [70], with a thermal conductivity significantly lower than that required for daily thermal storage.

Using the well-known equation of Gibson and Ashby [71] and neglecting the contribution of radiative transfer, quite low at room temperature:

$$\kappa = \phi \kappa_g + \frac{1}{3} \kappa_s (1 - \phi) \quad \text{Eq. 14}$$

which describes the dependence of the thermal conductivity κ of a foam on its porosity ϕ , κ_g being the thermal conductivity of the gas saturating the porosity ($0.0257 \text{ W m}^{-1} \text{ K}^{-1}$ for air at room temperature), it is possible to recalculate the thermal conductivity κ_s of the solid skeleton. With $\phi = 0.2$ (see again Table S2), one finds $\kappa_s = 45.2 \text{ W m}^{-1} \text{ K}^{-1}$.

Eq. (12) and Eq. (13) also apply to thermal conductivity. Therefore, using the average thermal conductivity values of isostatic graphite, $180 \text{ W m}^{-1} \text{ K}^{-1}$ [60,66] and phenolic resin-derived glassy carbon, $3.5 \text{ W m}^{-1} \text{ K}^{-1}$ [67], we find an effective thermal conductivity for the non-porous carbon-carbon composite of $60 \text{ W m}^{-1} \text{ K}^{-1}$. This value is also of the same order of magnitude as that, $45.2 \text{ W m}^{-1} \text{ K}^{-1}$, determined by application of Eq. (14).

It was shown that, to be effective in seasonal thermal storage using sugar alcohols as phase-change materials, the porosity of porous carbon matrices should be at least 80% and their thermal conductivity between 3 and $10 \text{ W m}^{-1} \text{ K}^{-1}$ [70]. Reusing Eq. (4) with the previously found value for κ_s , the predicted thermal conductivity for 3D-printed carbon with porosity $\phi = 0.8$ is then equal to $3 \text{ W m}^{-1} \text{ K}^{-1}$. Considering that the conductivity behind these values was measured in the out-of-plane direction, thus in the least favorable direction, it can be assumed that the present carbons meet the required specifications even better for the seasonal thermal energy storage application.

4. Conclusion

For the first time, graphite-carbon structures with triply periodic minimal surfaces were successfully produced via binder jetting of graphite-carbon black powders followed by polymer infiltration and pyrolysis with a furan resin. The tomography confirmed the good

resolution achieved and the reproducibility of the 3D printing process and, despite a linear shrinkage of 10.5%, the parts retained their complex shapes intact after pyrolysis. The use of phenolic resin as a binder and furan resin for densification resulted in compact structures composed of highly disordered carbon matrix binding well-crystallized graphite grains. X-ray diffraction analysis demonstrated the coexistence of both phases in the material, with the carbon matrix and graphite accounting for approximately 30 and 70 vol% of the composite, respectively.

The mechanical properties were excellent; in particular, a maximum compressive strength of 27.10 MPa was determined and found to be high with respect to the literature, considering that the samples had a geometric porosity of about 62% and a material's intrinsic porosity of 20%. The oxidation tests revealed a preferential oxidation of the disordered carbon matrix wrapping the graphite grains compared to the oxidation of the graphite itself, occurring at higher temperatures. Nevertheless, the overall oxidation resistance remained exceptionally high. Finally, the activation energies were found to be intermediate between those of pure graphite and pure amorphous carbon, which is typical of amorphous carbon-graphite composites.

Furthermore, considering that the electrical conductivity of the carbon backbone, which is intrinsically porous, can reach about 350 S cm^{-1} , and that its thermal conductivity is at least equal to about $45.2 \text{ W m}^{-1} \text{ K}^{-1}$, these new 3D-printed carbons are potentially useable as Joule heating elements and as encapsulation matrices for phase change materials for seasonal thermal storage. Overall, these findings contribute to a better understanding of these composite materials shaped by additive manufacturing.

CRediT authorship contribution statement

Marco Pelanconi: Investigation, Writing – original draft, Writing – review & editing. **Pauline Blyweert:** Investigation, Writing – original draft, Writing – review & editing. **Giovanni Bianchi:** Investigation, Writing – review & editing. **Vincent Nicolas:** Supervision, Writing – review & editing. **Davide Viganò:** Investigation, Writing – review & editing. **Samuele Bottacin:** Investigation, Writing – review & editing. **Vanessa Fierro:** Investigation, Writing – review & editing. **Alain Celzard:** Supervision, Funding acquisition, Writing – original draft, Writing – review & editing. **Alberto Ortona:** Conceptualization, Supervision, Funding acquisition, Writing – original draft, Writing – review & editing.

Declaration of competing interest

The authors declare that they have no known competing financial interests or personal relationships that could have appeared to influence the work reported in this paper.

Acknowledgement

SUPSI wishes to thank the Innosuisse national program for financing this research under project agreement number “2155007844”, “Heat and mass exchanger for absorption and desorption systems with engineered ceramic architectures produced by additive manufacturing”. Part of the work was also sponsored by the NATO Science for Peace and Security Program (Grant G5697 CERTAIN “Globular carbon-based structures and metamaterials for enhanced electromagnetic protection”). The authors thank Julien Lallemand, teaching and research assistant at ENSTIB (University of Lorraine), for giving us access to the tomograph used in this work. Finally, the authors greatly acknowledge IMERYS Graphite & Carbon, Switzerland, for providing the graphite and CB powders, with useful suggestions on how to employ them, and for measuring the electrical and thermal properties of the 3D-printed carbons and providing us with the corresponding data.

Appendix A. Supplementary data

Supplementary data to this article can be found online at <https://doi.org/10.1016/j.carbon.2023.118252>.

References

- [1] P. Blyweert, V. Nicolas, V. Fierro, A. Celzard, 3D printing of carbon-based materials : a review, *Carbon* 183 (2021) 449–485, <https://doi.org/10.1016/j.carbon.2021.07.036>.
- [2] K. Fu, Y. Yao, J. Dai, L. Hu, Progress in 3D printing of carbon materials for energy-related applications, *Adv. Mater.* 29 (2017), 1603486, <https://doi.org/10.1002/adma.201603486>.
- [3] J.L. Alves, L. Santana, E.M. Ocaña Garzón, Chapter 10 - binder jetting, in: J. Izdebska-Podsiady (Ed.), *Polymers for 3D Printing*, William Andrew Publishing, 2022, pp. 113–125, <https://doi.org/10.1016/B978-0-12-818311-3.00010-0>.
- [4] S.J. Trenfield, C.M. Madla, A.W. Basit, S. Gaisford, Binder jet printing in pharmaceutical manufacturing, in: A.W. Basit, S. Gaisford (Eds.), *3D Printing of Pharmaceuticals*, Springer International Publishing, Cham, 2018, pp. 41–54, https://doi.org/10.1007/978-3-319-90755-0_3.
- [5] X. Chen, S. Wang, J. Wu, S. Duan, X. Wang, X. Hong, et al., The application and challenge of binder jet 3D printing technology in pharmaceutical manufacturing, *Pharmaceutics* 14 (2022) 2589, <https://doi.org/10.3390/pharmaceutics14122589>.
- [6] A. Azhari, E. Marzbanrad, D. Yilman, E. Toyserkani, M.A. Pope, Binder-jet powder-based additive manufacturing (3D printing) of thick graphene-based electrodes, *Carbon* 119 (2017) 257–266, <https://doi.org/10.1016/j.carbon.2017.04.028>.
- [7] J.P. Kelly, L.R. Finkenauer, P. Roy, J.K. Stolaroff, D.T. Nguyen, M.S. Ross, et al., Binder jet additive manufacturing of ceramic heat exchangers for concentrating solar power applications with thermal energy storage in molten chlorides, *Addit. Manuf.* 56 (2022), 102937, <https://doi.org/10.1016/j.addma.2022.102937>.
- [8] J. Thomas, M. Banda, W. Du, W. Yu, A. Chuang, D.M. France, et al., Development of a silicon carbide ceramic based counter-flow heat exchanger by binder jetting and liquid silicon infiltration for concentrating solar power, *Ceram. Int.* 48 (2022) 22975–22984, <https://doi.org/10.1016/j.ceramint.2022.04.269>.
- [9] V. Popov, A. Fleisher, G. Muller-Kamskii, S. Avraham, A. Shishkin, A. Katz-Demyanetz, et al., Novel hybrid method to additively manufacture denser graphite structures using Binder Jetting, *Sci. Rep.* 11 (2021) 2438, <https://doi.org/10.1038/s41598-021-81861-w>.
- [10] S. Saunders, CARBOPRINT: ExOne Using Binder Jet 3D Printing to Produce Carbon and Graphite Components with SGL Group, 3DPrint.Com, 2018. <https://3dprint.com/205381/exone-sgl-group-carboprint/>. (Accessed 28 February 2023).
- [11] H. Miyajima, J.M. Akbar, L. Yang, Fabrication and characterization of Graphite/Nylon 12 composite via Binder Jetting additive manufacturing process, in: *Austin (USA)*, 2017.
- [12] E. Fitzer, L.M. Manocha, Carbon Reinforcements and Carbon/Carbon Composites, Springer, Berlin, Heidelberg, 1998, <https://doi.org/10.1007/978-3-642-58745-0>.
- [13] Y. Zhang, R. Wang, Sorption thermal energy storage: concept, process, applications and perspectives, *Energy Storage Mater.* 27 (2020) 352–369, <https://doi.org/10.1016/j.ensm.2020.02.024>.
- [14] F. Mikšik Chairunnisa, T. Miyazaki, K. Thu, J. Miyawaki, K. Nakabayashi, et al., Enhancing water adsorption capacity of acorn nutshell based activated carbon for adsorption thermal energy storage application, *Energy Rep.* 6 (2020) 255–263, <https://doi.org/10.1016/j.egyres.2020.11.038>.
- [15] M. Dudita, X. Daguenet-Frick, P. Gantenbein, Seasonal thermal energy storage with aqueous sodium hydroxide – experimental methods for increasing the heat and mass transfer by improving surface wetting, in: *Palma (Mallorca)*, 2016, <https://doi.org/10.18086/eurosun.2016.03.13>.
- [16] M. Sharif Sh, F. Golestani-Fard, H. Sarpoolaky, Improvement of water/resin wettability of graphite using carbon black nano particles coating via ink media, *J. Alloys Compd.* 482 (2009) 361–365, <https://doi.org/10.1016/j.jallcom.2009.04.019>.
- [17] J.W. Oh, Y. Seong, S.J. Park, Effect of nanoparticles in bimodal powder on physical and mechanical properties of powder injection molded parts, *J. Mater. Process. Technol.* 262 (2018) 503–510, <https://doi.org/10.1016/j.jmatprotec.2018.07.012>.
- [18] R.E. Ayala, P.A. Hartley, G.D. Parfitt, The relevance of powder/liquid wettability to the cohesiveness of carbon black agglomerates, *Part. Part. Syst. Char.* 3 (1986) 26–31, <https://doi.org/10.1002/ppsc.19860030106>.
- [19] ISO/ASTM, Standard test method for air oxidation of carbon and graphite in the kinetic regime- ASTM d7542-15. <https://www.astm.org/d7542-09.html>, 2015. (Accessed 28 February 2023).
- [20] C.I. Contescu, S. Azad, D. Miller, M.J. Lance, F.S. Baker, T.D. Burchell, Practical aspects for characterizing air oxidation of graphite, *J. Nucl. Mater.* 381 (2008) 15–24, <https://doi.org/10.1016/j.jnucmat.2008.07.020>.
- [21] J. Rouquerol, P. Llewellyn, F. Rouquerol, Is the bet equation applicable to microporous adsorbents? in: P.L. Llewellyn, F. Rodriguez-Reinoso, J. Rouquerol, N. Seaton (Eds.), *Studies in Surface Science and Catalysis Elsevier*, 2007, pp. 49–56, [https://doi.org/10.1016/S0167-2991\(07\)80008-5](https://doi.org/10.1016/S0167-2991(07)80008-5).
- [22] M. Thommes, K. Kaneko, A.V. Neimark, J.P. Olivier, F. Rodriguez-Reinoso, J. Rouquerol, et al., Physisorption of gases, with special reference to the evaluation of surface area and pore size distribution (IUPAC Technical Report), *Pure Appl. Chem.* 87 (2015) 1051–1069, <https://doi.org/10.1515/pac-2014-1117>.

- [23] J. Jagiello, J.P. Olivier, Carbon slit pore model incorporating surface energetical heterogeneity and geometrical corrugation, *Adsorption* 19 (2013) 777–783, <https://doi.org/10.1007/s10450-013-9517-4>.
- [24] P.A. Webb, C. Orr, *Analytical Methods in Fine Particle Technology*, Micromeritics Instrument Corporation, 1997.
- [25] P.A. Webb, *Volume and Density Determinations for Particle Technologists*, vol. 2, 2001, 01.
- [26] J.B. Wade, G.P. Martin, D.F. Long, An assessment of powder pycnometry as a means of determining granule porosity, *Pharmaceut. Dev. Technol.* 20 (2015) 257–265, <https://doi.org/10.3109/10837450.2013.860550>.
- [27] C. Beny-Bassez, J.N. Rouzaud, Characterization of carbonaceous materials by correlated electron and optical microscopy and Raman microspectroscopy, *Scanning Electron. Microsc.* (1984) 1985, <https://digitalcommons.usu.edu/electron/vol1985/iss1/11>.
- [28] D.S. Knight, W.B. White, Characterization of diamond films by Raman spectroscopy, *J. Mater. Res.* 4 (1989) 385–393, <https://doi.org/10.1557/JMR.1989.0385>.
- [29] Y. Wang, D.C. Alsmeyer, R.L. McCreery, Raman spectroscopy of carbon materials: structural basis of observed spectra, *Chem. Mater.* 2 (1990) 557–563, <https://doi.org/10.1021/cm00011a018>.
- [30] A. Cuesta, P. Dhamelincourt, J. Laureyns, A. Martínez-Alonso, J.M.D. Tascón, Raman microprobe studies on carbon materials, *Carbon* 32 (1994) 1523–1532, [https://doi.org/10.1016/0008-6223\(94\)90148-1](https://doi.org/10.1016/0008-6223(94)90148-1).
- [31] A.C. Ferrari, D.M. Basko, Raman spectroscopy as a versatile tool for studying the properties of graphene, *Nat. Nanotechnol.* 8 (2013) 235–246, <https://doi.org/10.1038/nnano.2013.46>.
- [32] L.G. Cançado, K. Takai, T. Enoki, M. Endo, Y.A. Kim, H. Mizusaki, et al., General equation for the determination of the crystallite size L_a of nanographite by Raman spectroscopy, *Appl. Phys. Lett.* 88 (2006), 163106, <https://doi.org/10.1063/1.2196057>.
- [33] P. Snapp, J.M. Kim, C. Cho, J. Leem, M.F. Haque, S. Nam, Interaction of 2D materials with liquids: wettability, electrochemical properties, friction, and emerging directions, *NPG Asia Mater.* 12 (2020) 1–16, <https://doi.org/10.1038/s41427-020-0203-1>.
- [34] Z. Li, Y. Wang, A. Kozbial, G. Shenoy, F. Zhou, R. McGinley, et al., Effect of airborne contaminants on the wettability of supported graphene and graphite, *Nat. Mater.* 12 (2013) 925–931, <https://doi.org/10.1038/nmat3709>.
- [35] L. Shi, Q. Gao, Y. Wu, High performance oxide functionalized nitrogen-doped mesocellular carbon foam for biosensor construction, *Electroanalysis* 21 (2009) 715–722, <https://doi.org/10.1002/elan.200804469>.
- [36] J. Jeevahan, M. Chandrasekaran, G. Britto Joseph, R.B. Durairaj, G. Mageshwaran, Superhydrophobic surfaces: a review on fundamentals, applications, and challenges, *J. Coating Technol. Res.* 15 (2018) 231–250, <https://doi.org/10.1007/s11998-017-0011-x>.
- [37] M. Saget, C.F. de Almeida, V. Fierro, A. Celzard, G. Delaplace, V. Thomy, et al., A critical review on surface modifications mitigating dairy fouling, *Compr. Rev. Food Sci. Food Saf.* 20 (2021) 4324–4366, <https://doi.org/10.1111/1541-4337.12794>.
- [38] M.R. Ammar, J.-N. Rouzaud, How to obtain a reliable structural characterization of polished graphitized carbons by Raman microspectroscopy, *J. Raman Spectrosc.* 43 (2012) 207–211, <https://doi.org/10.1002/jrs.3014>.
- [39] J.-C. Rietsch, P. Brender, J. Dentzer, R. Gadiou, L. Vidal, C. Vix-Guterl, Evidence of water chemisorption during graphite friction under moist conditions, *Carbon* 55 (2013) 90–97, <https://doi.org/10.1016/j.carbon.2012.12.013>.
- [40] R. Brezny, D.J. Green, Uniaxial strength behavior of brittle cellular materials, *J. Am. Ceram. Soc.* 76 (1993) 2185–2192, <https://doi.org/10.1111/j.1151-2916.1993.tb07753.x>.
- [41] M. Letellier, C. Delgado-Sanchez, M. Khelifa, V. Fierro, A. Celzard, Mechanical properties of model vitreous carbon foams, *Carbon* 116 (2017) 562–571, <https://doi.org/10.1016/j.carbon.2017.02.020>.
- [42] J. He, H. Wu, L. Zhong, Q. Zhong, Q. Yang, X. Ye, et al., Mechanical properties and thermal conductivity of lightweight and high-strength carbon-graphite thermal insulation materials, *J. Mater. Sci.* 57 (2022) 4166–4179, <https://doi.org/10.1007/s10853-021-06862-6>.
- [43] R. Llamas-Unzueta, J.A. Menéndez, M. Suárez, A. Fernández, M.A. Montes-Morán, From whey roasting to custom 3D porous carbons, *Addit. Manuf.* 59 (2022), 103083, <https://doi.org/10.1016/j.addma.2022.103083>.
- [44] P. Blyweert, V. Nicolas, J. Macutkevicius, V. Fierro, A. Celzard, Tannin-based resins for 3D printing of porous carbon architectures, *ACS Sustainable Chem. Eng.* (2022), <https://doi.org/10.1021/acssuschemeng.2c01686>.
- [45] P. Blyweert, V. Nicolas, V. Fierro, A. Celzard, Experimental design optimisation of tannin-acrylate photocurable resins for 3D printing of biobased porous carbon architectures, *Molecules* (2022), <https://doi.org/10.3390/molecules27072091>.
- [46] V.M. Samoilov, D.V. Shilo, Effect of grain size on the thermal expansion of isotropic synthetic graphites, *Inorg. Mater.* 41 (2005) 1283–1288, <https://doi.org/10.1007/s10789-005-0302-y>.
- [47] P. Hidnert, W.T. Sweeney, *Thermal Expansion of Graphite*, 1927, p. 21.
- [48] Htw Germany, (n.d.), <http://www.htw-germany.com> (accessed February 8, 2023).
- [49] Y.S. Touloukian, R.K. Kirby, E.R. Taylor, T.Y.R. Lee, *Thermophysical Properties of Matter - the TPRC Data Series*, vol. 13, Thermal Expansion - Nonmetallic Solids, 1977, <https://www.scinapse.io/papers/1593236975>.
- [50] ERG aerospace | home of patented duocel foam | metal foam, <https://Ergaerospace.Com/>. (Accessed 8 February 2023). <https://ergaerospace.com/> (n.d.).
- [51] L. Xiaowei, R. Jean-Charles, Y. Suyuan, Effect of temperature on graphite oxidation behavior, *Nucl. Eng. Des.* 227 (2004) 273–280, <https://doi.org/10.1016/j.nucengdes.2003.11.004>.
- [52] R.E. Smith, J.J. Kane, W.E. Windes, Determining the acute oxidation behavior of several nuclear graphite grades, *J. Nucl. Mater.* 545 (2021), 152648, <https://doi.org/10.1016/j.jnucmat.2020.152648>.
- [53] X. Zhou, C.I. Contescu, X. Zhao, Z. Lu, J. Zhang, Y. Katoh, et al., Oxidation behavior of matrix graphite and its effect on compressive strength, *Science and Technology of Nuclear Installations* 2017 (2017), e4275375, <https://doi.org/10.1155/2017/4275375>.
- [54] P. Blyweert, V. Nicolas, V. Fierro, A. Celzard, 3D-printed carbons with improved properties and oxidation resistance, *ACS Sustainable Chem. Eng.* (2023).
- [55] A. Celzard, J.F. Maréché, F. Payot, G. Furdin, Electrical conductivity of carbonaceous powders, *Carbon* 40 (2002) 2801–2815, [https://doi.org/10.1016/S0008-6223\(02\)00196-3](https://doi.org/10.1016/S0008-6223(02)00196-3).
- [56] I.L. Spain, *The electronic properties of graphite*, in: *Chemistry and Physics of Carbon*, Marcel Dekker Inc., New York, 1973, pp. 1–150.
- [57] M.F. Ashby, A. Evans, N.A. Fleck, L.J. Gibson, J.W. Hutchinson, H.N.G. Wadley, *Metal Foams: A Design Guide*, first ed., 2000, Boston.
- [58] F.G. Cuevas, J.M. Montes, J. Cintas, P. Urban, Electrical conductivity and porosity relationship in metal foams, *J. Porous Mater.* 16 (2009) 675–681, <https://doi.org/10.1007/s10934-008-9248-1>.
- [59] R. Landauer, Electrical conductivity in inhomogeneous media, *AIP Conf. Proc.* 40 (1978) 2–45, <https://doi.org/10.1063/1.311510>.
- [60] A. Karvatskii, S. Leleka, T. Lazarev, A. Pedchenko, Investigation of the current state of isostatic graphite production technology, *Technol. Audit Prod. Reserves* 2 (2017) 16–21, <https://doi.org/10.15587/2312-8372.2017.98125>.
- [61] L. Soukup, I. Gregora, L. Jastrabik, A. Koňáková, Raman spectra and electrical conductivity of glassy carbon, *Mater. Sci. Eng., B* 11 (1992) 355–357, [https://doi.org/10.1016/0921-5107\(92\)90240-A](https://doi.org/10.1016/0921-5107(92)90240-A).
- [62] A. Szczurek, V. Fierro, A. Plyushch, J. Macutkevicius, P. Kuzhir, A. Celzard, Structure and electromagnetic properties of cellular glassy carbon monoliths with controlled cell size, *Materials* 11 (2018) 709, <https://doi.org/10.3390/ma11050709>.
- [63] S. Picard, D.T. Burns, P. Roger, Determination of the specific heat capacity of a graphite sample using absolute and differential methods, *Metrologia* 44 (2007) 294, <https://doi.org/10.1088/0026-1394/44/5/005>.
- [64] M. Letellier, *Optimisation de mousses de carbone dérivées de tannin par l'étude et la modélisation de leurs propriétés physiques*, PhD Thesis, Université de Lorraine, 2015.
- [65] M.F. Ashby (Ed.), *Materials Selection in Mechanical Design*, fourth ed., Butterworth-Heinemann, Oxford, 2011 <https://doi.org/10.1016/B978-1-85617-663-7.00026-6>.
- [66] P. Delhaes, *Carbon Science and Technology: from Energy to Materials*, John Wiley & Sons, 2012.
- [67] M. Bastick, P. Chiche, J. Rappeneau, *La texture des carbones*, in: *Groupe Français d'étude des carbones*, Masson et Cie, Paris, 1965, p. 208.
- [68] A.-T. Chien, S. Cho, Y. Joshi, S. Kumar, Electrical conductivity and Joule heating of polyacrylonitrile/carbon nanotube composite fibers, *Polymer* 55 (2014) 6896–6905, <https://doi.org/10.1016/j.polymer.2014.10.064>.
- [69] P. Jana, E. Palomo del Barrio, M. Dubois, M. Duquesne, A. Godin, C. Vautrin-Ul, et al., Hydrophobised carbon foams for improved long-term seasonal solar thermal energy storage, *Sol. Energy Mater. Sol. Cells* 220 (2021), 110849, <https://doi.org/10.1016/j.solmat.2020.110849>.
- [70] P. Jana, E. Palomo del Barrio, V. Fierro, G. Medjahdi, A. Celzard, Design of carbon foams for seasonal solar thermal energy storage, *Carbon* 109 (2016) 771–787, <https://doi.org/10.1016/j.carbon.2016.08.048>.
- [71] L.J. Gibson, M.F. Ashby, *Cellular Solids: Structure and Properties*, second ed., Cambridge University Press, 1997 <https://doi.org/10.1017/CBO9781139878326>.